Chinese Chemical Letters 36 (2025) 110700

Contents lists available at ScienceDirect

Chinese Chemical Letters

journal homepage: www.elsevier.com/locate/cclet

# Molecular engineering of dibenzo-heterocyclic core based hole-transporting materials for perovskite solar cells

Yajie Yang, Mengde Zhai, Haoxin Wang, Cheng Chen*, Ziyang Xia, Chengyang Liu, Yi Tian*, Ming Cheng

*Institute for Energy Research, Jiangsu University, Zhenjiang 212013, China*

ARTICLE INFO

*Article history:*
Received 21 July 2024
Revised 27 November 2024
Accepted 28 November 2024
Available online 6 December 2024

*Keywords:*
Heteroatom effect
Dibenzo-heterocycle
Hole transport material
Perovskite solar cells
Passivation effect

ABSTRACT

Heterocyclic compounds play an important role in organic hole transport materials (HTMs) for perovskite solar cells (PSCs). Herein, a series of linear D-$\pi$-D HTMs (O–CBz, S-CBz, SO2-CBz) with different dibenzo-heterocycles core (dibenzofuran, dibenzothiophene, dibenzothiophene sulfone) were designed and synthesized, and their applications in PSCs were investigated. The intrinsic properties (CV, UV–vis, hole mobility and conductivity) were systematically investigated, demonstrating that all three materials are suitable HTMs for planar n-i-p type PSCs. Benefiting from the excellent hole mobility and conductivity, good film forming ability, and outstanding charge extraction and transport capability of S-CBz, $FAPbI_3$-based PSCs using S-CBz as HTM achieved a PCE of 25.0%, which is superior to that of Spiro-OMeTAD-based PSCs fabricated under the same conditions (23.9%). Furthermore, due to the interaction between S and $Pb^{2+}$, S-CBz-based PSC devices exhibited improved stability. This work demonstrates that dibenzothiophene-based architectures are promising candidates for high-performance HTMs in perovskite solar cell architectures.



Perovskite materials have attracted wide attention in the field of photovoltaics due to their excellent performance. At present, the power conversion efficiency (PCE) of single-junction perovskite solar cells (PSCs) has surpassed 26%, which is comparable to the PCE of commercial crystalline silicon solar cells [1–8]. In traditional perovskite solar cells, the hole transport material (HTM) plays a crucial role in blocking electrons, extracting and transporting holes, and protecting the perovskite active layer. Therefore, developing efficient and stable HTMs is a key strategy to improve the power conversion efficiency and long-term operational stability of PSC devices [9–12]. Organic molecules are often used as hole transport layers due to their well-defined structures, high molecular reproducibility, ease of purification, and compatibility to spin coating during device fabrication [13,14]. To date, 2,2′′,7,7′′-tetrakis[*N*,*N*-di(4-methoxyphenyl)amino]-9,9′-spirobifluorene (Spiro-OMeTAD) is the most commonly used HTM in n-i-p type perovskite devices. However, its large-scale commercial application is hampered by inherent disadvantages of orthometric molecular structure such as complex and highly cost synthetic procedure and low charge carrier mobility. Therefore, it is necessary to develop new types of HTMs [15–21]. In general, the core or bridge of HTMs greatly affects their photophysical, electrochemical, and photovoltaic properties [22–24]. By employing planar core unit with large $\pi$-conjunction, the hole mobility and conductivity of HTMs can be well improved, qualifying them as dopant-free HTMs [25–30]. The effects of heteroatoms on tuning energy level, changing intermolecular or intramolecular interactions and passivation of perovskite surface defects has been long recognized and many heterocyclic based HTMs that comparable to Spiro-OMeTAD have been reported [31–34]. Introduction of a sulfone group on HTM backbone is reported to be an efficient way to develop HTMs, and a variety of sulfone-containing core structures can be developed. By doing so, a systematic comparation of the effects of oxygen, sulfur and sulfone in different chemical environment on the material properties and performance of PSC devices could be well conducted.

Considering the above, we design and develop a series of dibenzo-heterocyclic core based D-$\pi$-D-type hole-transporting materials O–CBz, S-CBz, and SO2-CBz, in which dibenzo[*b*,*d*]furan (DBF), dibenzo[*b*,*d*]thiophene (DBT), and dibenzothiophene sulfone (DBTS) as the core and *N*3,*N*6-bis(di-4-anisylamino)-9*H*-carbazole (DAnCBZ) as the end-capping unit at the 3- and 7-positions of the core, respectively. The oxygen, sulfur and sulfone are supposed to coordinate with $Pb^{2+}$ and reduce the defects of perovskite layer [35–38]. The $\pi$-electrons are delocalized over the $\pi$-conjugated carbazole moieties *via* the lone pairs of electrons at the N atoms in DAnCBZ. In addition, the use of DAnCBZ as a weapon plays an

* Corresponding authors.
*E-mail addresses:* chencheng@ujs.edu.cn (C. Chen), tianyi@ujs.edu.cn (Y. Tian).

https://doi.org/10.1016/j.cclet.2024.110700
1001-8417/

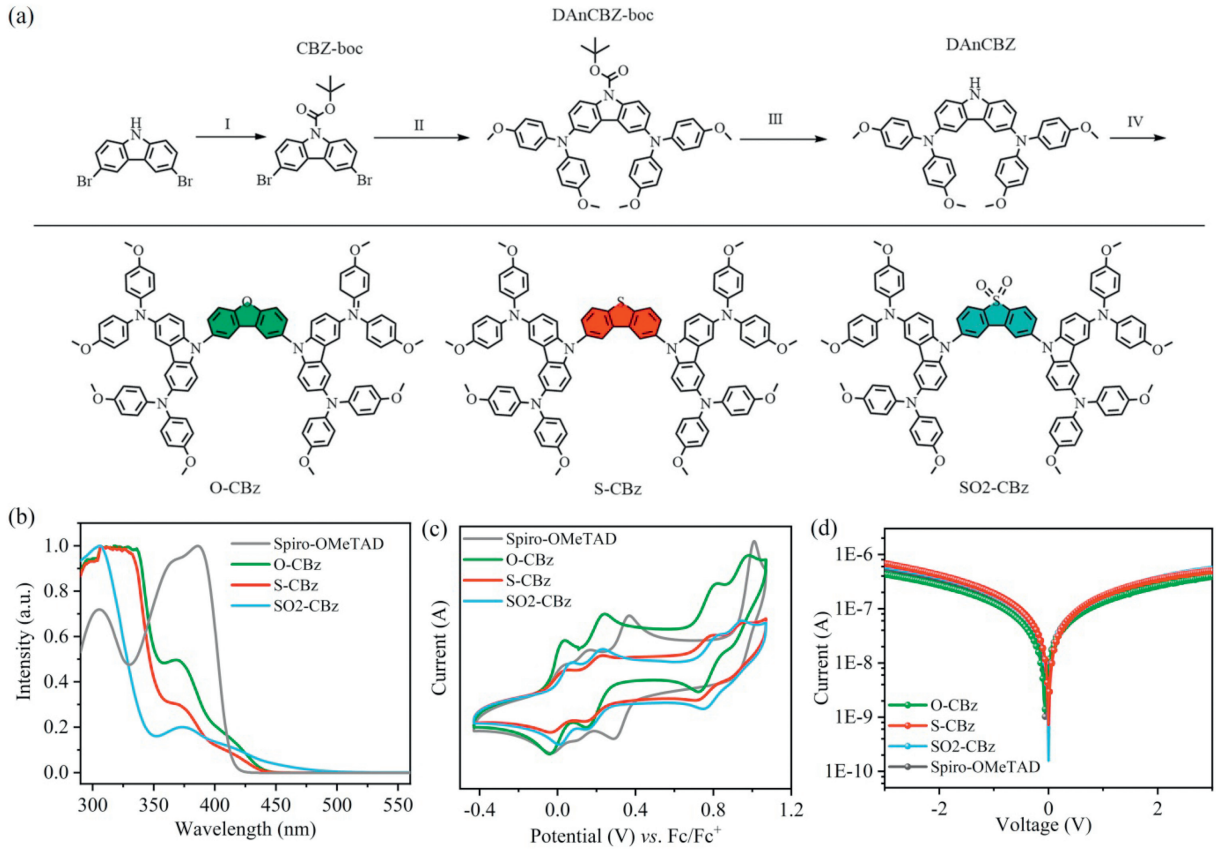


**Fig. 1.** (a) Synthetic route for the preparation of O–CBz S-CBz and SO2-CBz. (I) THF, 1 h; (II) $Pd_2(dba)_3$, $[(t\text{-}Bu)_3PH]BF_4$, *t*-BuONa, toluene, 120 °C, 12 h; (III) *t*-BuOK, 120 °C, 2 h; (IV) $Pd_2(dba)_3$, $[(t\text{-}Bu)_3PH]BF_4$, *t*-BuONa, toluene, 120 °C, 12 h. (b) Normalized UV–vis spectra and photoluminescence spectra of O–CBz, S-CBz, SO2-CBz and Spiro-OMeTAD in $CH_2Cl_2$ solution. (c) CV results of O–CBz, S-CBz, SO2-CBz and Spiro-OMeTAD in $CH_2Cl_2$ solution. (d) The hole mobilities of O–CBz, S-CBz, SO2-CBz and Spiro-OMeTAD.

important role in tuning energy levels, enhancing material stability, and endowing good optical properties. In this work, we systematically investigate the effects of heteroatom variation on the optical and electrochemical properties of HTMs through a series of techniques and further explore the influence on photovoltaic properties of corresponding PSCs.

The three designed HTMs, O–CBz, S-CBz, and SO2-CBz, can be simply synthesized by Buchwald-Hartwig coupling reaction and Suzuki-Miyaura reaction with high yields, and detailed synthetic routes are described in Fig. 1a. The obtained products were comprehensively identified using a variety of spectroscopic techniques, including $^1$H nuclear magnetic resonance ($^1$H NMR), $^1$C nuclear magnetic resonance ($^1$C NMR) and high-resolution mass spectrometry (HRMS) (Figs. S1-S9 in Supporting information).

The photophysical properties of the studied molecules in dichloromethane solution were clarified as indicated in Fig. 1b, and detailed data are provided in Table S1 (Supporting information). O–CBz, S-CBz, and SO2-CBz all exhibit three distinct absorption bands in the UV–vis region, and all obvious redshifted compared to Spiro-OMeTAD. O–CBz, S-CBz, and SO2-CBz exhibit three absorption bands in the visible ultraviolet region. The first two bands, located at 306 and 369 nm, 307 and 368 nm, and 306 and 373 nm, respectively, are primarily attributed to $\pi$-$\pi^*$ electronic transitions within the HTM conjugated system. The longer wavelength band, observed at 413, 413 and 422 nm, is ascribed to intramolecular charge transfer (ICT) transitions. In addition, the presence of the strong electron-withdrawing effect of the sulfone group in SO2-CBz results in a 9 nm redshift in its absorption band compared to O–CBz and S-CBz [32]. The optical bandgaps were calculated as 2.79, 2.78, and 2.74 eV for O–CBz, S-CBz, and SO2-CBz, respectively, by using the formula $E_g = 1240/\lambda_{int}$, where $\lambda_{int}$ is the intersection point of the photoluminescence and UV–vis spectra. Those HTMs have smaller optical bandgaps than Spiro-OMeTAD (−2.96 eV). In addition, the cyclic voltammetry (CV) curves of the O–CBz, S-CBz, and SO2-CBz (Fig. 1c) exhibit three highly reversible oxidation potentials, indicative of exceptional electrochemical stability, corresponding to the formation of radical cation and dication quinone diimine of the carbazole moiety. The HOMO energy levels of O–CBz, S-CBz, and SO2-CBz are identified as −5.12, −5.12, and −5.14 eV, respectively. The HOMO of Spiro-OMeTAD was calculated as −5.12 eV in the same manner. The results indicate that these three HTMs match well with the perovskite energy levels. This conclusion can also be validated by ultraviolet photoelectron spectroscopy (UPS) (Figs. S11a-d in Supporting information). The lowest unoccupied molecular orbital (LUMO) energy levels of O–CBz, S-CBz, SO2-CBz, and Spiro-OMeTAD are calculated to be −2.33, −2.34, −2.40, and −2.16 eV according to the equation $E_{LUMO} = E_{HOMO} + E_g$, which are higher than the conduction band (CB) of perovskite, effectively reducing open-circuit voltage ($V_{OC}$) loss by preventing the movement of photogenerated electrons to the metal electrode and facilitating the transfer of holes from the perovskite layer to the metal electrode [39].

To assess the charge transport properties of HTMs with different dibenzo-heterocycles core, hole mobilities (Fig. 1d) were measured using the space charge limited current (SCLC) method, and the details are described in Supporting information. The hole mobilities of O–CBz, S-CBz, SO2-CBz, and Spiro-OMeTAD are calculated based on Mott-Gurney's law ($J = 9/8\mu\varepsilon_0\varepsilon_r V^2/D^3$) and summarized in Table S1. The reported HTMs show comparable hole mobility with Spiro-OMeTAD, and S-CBz ($\mu = 2.72 \times 10^{-4}$ cm$^2$ V$^{-1}$ s$^{-1}$) is

slightly higher than SO2-CBz ($\mu = 2.43 \times 10^{-4}$ cm$^2$ V$^{-1}$ s$^{-1}$), O–CBz ($\mu = 2.53 \times 10^{-4}$ cm$^2$ V$^{-1}$ s$^{-1}$) and Spiro-OMeTAD ($\mu = 2.66 \times 10^{-4}$ cm$^2$ V$^{-1}$ s$^{-1}$). The conductivities of the three HTMs shows consistent results with their hole mobilities (Fig. S11e in Supporting information).

To understand the effect of heteroatoms in dibenzo-pentacycles cores, the molecular front orbital distribution and electrostatic potential (ESP) were calculated using density functional theory (DFT) at the B3LYP/6–31G(d) level as shown in Fig. S12 (Supporting information). O–CBz, S-CBz and SO2-CBz show almost the same spin density distribution pattern with HOMO mainly delocalized at the dibenzo-heterocycles core and LUMO mainly on the DAnCBZ arms. In particular, the HOMO distribution of O–CBz and S-CBz is more delocalized over the DAnCBZ moiety than that of SO2-CBz, which may be attributed to the strong electron withdrawal property of the sulfonyl group. The closely related distributions of HOMO and LUMO facilitate charge hopping transport, indicating that O–CBz and S-CBz have greater hole extraction and transport potential compared to SO2-CBz, consistent with hole mobility test results. The HOMO values of O–CBz, S-CBz and SO2-CBz determined by density functional theory studies are −4.23, −4.23 and −4.37 eV, respectively, and LUMO energy levels are −1.33, −1.32 and −1.87 eV, respectively, which are consistent with cyclic voltammetry test results. ESP results show that the different core heteroatoms have significant effects on the electron cloud distribution of the molecule. The electron-rich regions of the three HTMs are mainly concentrated on the O and S heteroatoms, which is conducive to the coordination of HTMs with $Pb^{2+}$ in perovskite to reduce the generation of defects, while the electron-rich region of SO2-CBz is obviously concentrated on the sulfone group, which is mainly attributed to the acceptor strength of sulfone is higher than that of oxygen and sulfur atoms. Moreover, S-CBz shows smaller torsion angles than those of O–CBz (123.4°) and SO2-CBz (130.2°) (Fig. S13 in Supporting information), which is beneficial for the molecular skeleton stacks, leading to slightly higher hole mobility.

To fully explore their potential applications as HTLs in high-efficiency planar n-i-p-type PSCs, we first compare the $^1$H NMR of primary HTMs and HTMs/$PbI_2$ (Figs. S14a-c in Supporting information). After mixing with $PbI_2$, all the proton signals of O–CBz and S-CBz shift significantly to lower fields, while the proton signals of SO2-CBz shift only slightly, indicating that O–CBz and S-CBz would interact stronger as Lewis bases with uncoordinated $Pb^{2+}$ of perovskite layer [35]. HTMs/$PbI_2$ powders were prepared by drying a mixture of HTMs and $PbI_2$, and characterized by Fourier transform infrared (FTIR) spectroscopy. The results show that the characteristic C–O peak of O–CBz at 1235 cm$^{-1}$ undergoes a 4 cm$^{-1}$ shift to 1231 cm$^{-1}$ in the O–CBz/$PbI_2$ sample (Fig. S14d in Supporting information). Similarly, the characteristic C-S peak of S-CBz at 1224 cm$^{-1}$ exhibits a 11 cm$^{-1}$ shift to 1213 cm$^{-1}$ in the S-CBz/$PbI_2$ sample (Fig. S14e in Supporting information). The characteristic peak of O=S=O (1312 cm$^{-1}$) in SO2-CBz exhibits a 9 cm$^{-1}$ shift to 1321 cm$^{-1}$ in the S-CBz/$PbI_2$ sample (Fig. S14f in Supporting information). When $PbI_2$ is added, the characteristic peaks of O–CBz and SO2-CBz undergo minor shifts, likely due to the small initial ionization energy of oxygen. In contrast, the characteristic peak of S-CBz exhibits a pronounced shift, further confirming the strong interaction between S-CBz and $PbI_2$. X-ray photoelectron spectroscopy (XPS) was performed on FTO/$TiO_2$/$SnO_2$/$FAPbI_3$ and FTO/$TiO_2$/$SnO_2$/$FAPbI_3$/HTM thin films. As shown in Figs. S15a-c (Supporting information), a subtle shift was observed in the peaks of Pb 4f and I 3d after coating with HTMs. The Pb:I ratios of $FAPbI_3$ and $FAPbI_3$/O–CBz, $FAPbI_3$/S-CBz, and $FAPbI_3$/SO2-CBz samples were estimated to be 1:3.42, 1:2.93, 1:2.45 and 1:2.92, respectively. The lower Pb:I ratio of $FAPbI_3$/S-CBz suggests that the interaction between S-CBz and perovskite is stronger than that of other samples. Based on these results, it can be inferred that the passivation effect of S-CBz, which leads to reduced iodine vacancies, may result in fewer point defects, corresponding to the high fill factor (*FF*) observed in S-CBz-based devices.

To explore the film forming properties of O–CBz, S-CBz and SO2-CBz, we performed scanning electron microscopy (SEM) and atomic force microscopy (AFM) measurements. The target hole transport layer was spin-coated on top of the mixed-cation perovskite from a precursor solution containing dopants [lithium bis(trifluoromethanesulfonyl)imide (LiTFSI) and 4–*tert*-butylpyridine (*t*BP)] with a structure of glass/FTO/c-$TiO_2$/$SnO_2$/$FAPbI_3$/HTMs. It can be clearly seen from the SEM that there are tiny pores on the surface of O–CBz and SO2-CBz, probably due to their poor film formation properties, while the surface of S-CBz is smooth (Fig. S16 in Supporting information). The existence of pinholes makes it easier for the metal electrode to contact the perovskite directly, which will affect the transmission of charge, form defects, increase hole recombination, and correspondingly lead to more serious $V_{OC}$ loss and lower performance. At the same time, from AFM image analysis (Figs. S17a and b in Supporting information), we infer that the perovskite exhibits a rough surface with a high root mean square (RMS) value (43 nm), while the perovskite/O–CBz, perovskite/S-CBz, and perovskite/SO2-CBz show relatively smooth surfaces, with RMS values of 16.5, 12.6, and 16.8 nm, respectively. The uniform coverage and RMS attenuation signal indicate that the interface contact between the perovskite/HTL is beneficial to device performance.

To investigate the effect of molecular structure of different core heteroatoms on the photovoltaic performance of PSCs, typical planar n-i-p devices were fabricated by employing different molecules as HTMs based on previous reports. Detailed fabrication procedures are described in Supporting information, and cross-sectional image of the device is shown in Fig. S18 (Supporting information), and the PSC architecture of devices is shown in Fig. 2a. Extensive studies have shown that the amount of HTMs deposited has a great influence on device performance. In this work, we investigated the effect of HTMs concentration on the photovoltaic performance of PSCs. To compare device performance fabricated from different materials in different batches, conventional Spiro-OMeTAD doped devices were fabricated as references. Detailed average photovoltaic parameters such as $V_{OC}$, short-circuit current ($J_{SC}$), FF and PCE are summarized in Tables S2-S4 (Supporting information). For the three HTMs, when the concentration is above 65 mg/mL, the PCEs of the PSCs are generally lower, which may be due to the fact that too thick hole transport layer would result in overlarge series resistance of PSCs. Based on 60 mg/mL S-CBz and 73 mg/mL PSCs, negligible hysteresis is observed in both forward and reverse scans (Fig. 2b, Fig. S19c in Supporting information). After optimization, the best PCE of the device based on S-CBz is 25.0%, with a $V_{OC}$ of 1.18 V, $J_{SC}$ of 25.3 mA/cm$^2$ and FF of 83.7%, which is higher than that of Spiro-OMeTAD based device (23.9%), with a $V_{OC}$ of 1.15 V, $J_{SC}$ of 24.9 mA/cm$^2$ and *FF* of 83.3%. Optimized 60 mg/mL O–CBz and 65 mg/mL SO2-CBz champion devices exhibit efficiencies of 23.6% and 21.6%, respectively (Figs. S19a and b in Supporting information). And summary of the figures of merit of the PSCs in Table 1. Besides, we investigated the hysteresis effects on the photovoltaic performance of PSC devices base on different HTMs by analyzing forward/backward *J-V* curves. The hysteresis index (HI) of devices based on O–CBz, S-CBz, and SO2-CBz are 0.017, 0.004 and 0.042, respectively. The negligible hysteresis effect of S-CBz based device is mainly resulted from the lower film defect density and the higher efficiency of photogenerated charge extraction at the perovskite/HTM interface. The incident photon-to-electron conversion efficiency (IPCE) curves of the corresponding devices are shown in Fig. 2c. The integrated $J_{SC}^{cal}$ are 24.04, 24.26, 23.53 and 23.74 mA/cm$^2$, respectively for O–CBz, S-CBz, SO2-CBz and Spiro-OMeTAD, which are consistent with the values ob-

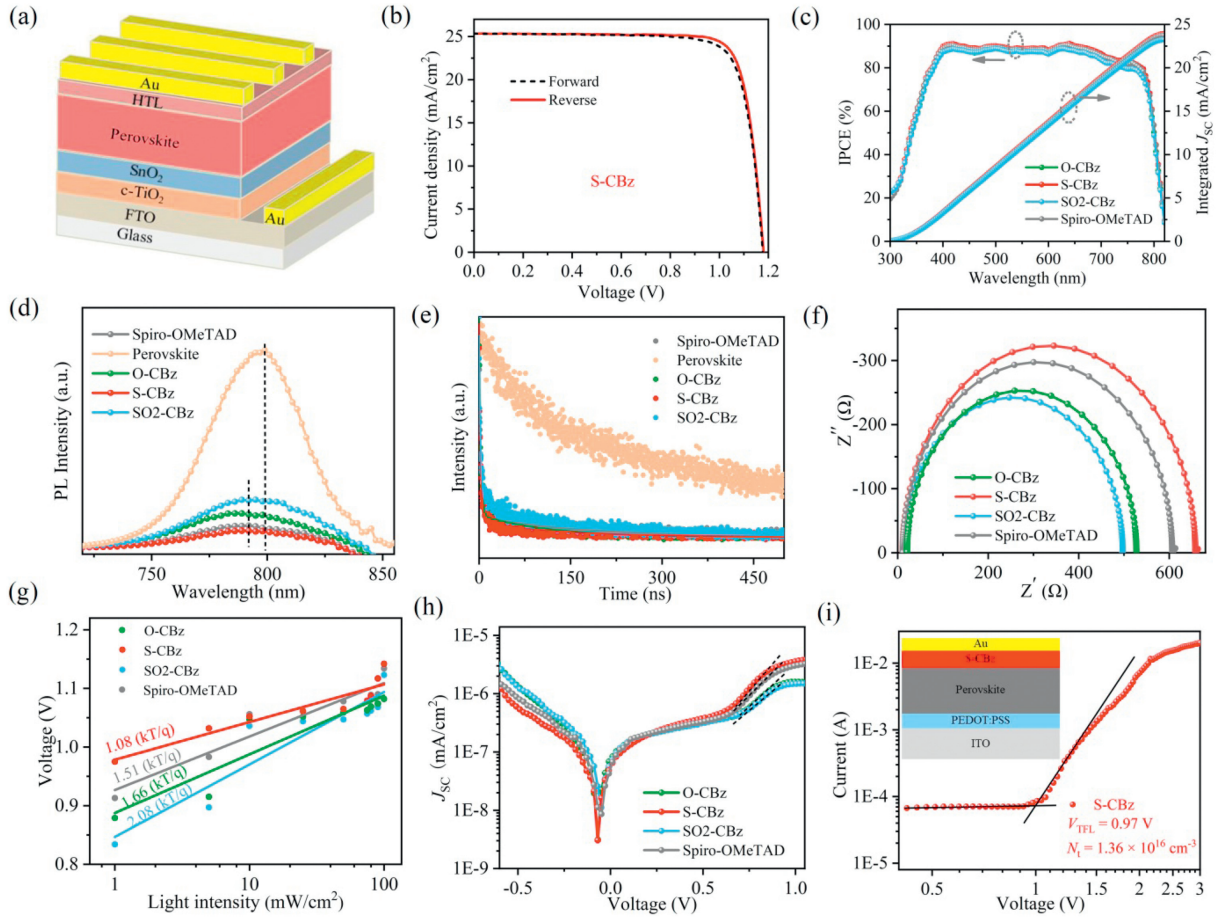


**Fig. 2.** (a) PSC architecture, (b) S-CBz measured by forward and reverse scans. (c) IPCE spectra of PSCs devices based on O–CBz, S-CBz, SO2-CBz and Spiro-OMeTAD. (d) PL and (e) TRPL spectra of the bare perovskite film and with O–CBz, S-CBz, SO2-CBz and Spiro-OMeTAD. (f) Nyquist plots of PSCs device based on both HTMs in dark condition with bias voltage 1.2 V. (g) $V_{OC}$ dependency of PSC device based on both HTMs on light intensity. (h) *J*–*V* curves for the PSCs with O–CBz, S-CBz, SO2-CBz and Spiro-OMeTAD measured under dark conditions. (i) Trap state density of hole-only devices with S-CBz. The inset shows the hole-only test structure.

**Table 1**
Summary of the figures of merit of the PSCs based on O–CBz, S-CBz, SO2-CBz and Spiro-OMeTAD under AM 1.5G illumination.

| HTL | Scan direction | $V_{OC}$ (V) | $J_{SC}$ (mA/cm$^2$) | *FF* (%) | PCE (%) | HI | $J_{SC}^{cal}$ (mA/cm$^2$) |
|---|---|---|---|---|---|---|---|
| O-CBz | Forward | 1.15 | 25.0 | 81.6 | 23.2 | 0.017 | 24.04 |
| | Reverse | 1.15 | 25.0 | 82.7 | 23.6 | | |
| S–CBz | Forward | 1.18 | 25.3 | 83.4 | 24.9 | 0.004 | 24.26 |
| | Reverse | 1.18 | 25.3 | 83.7 | 25.0 | | |
| SO2-CBz | Forward | 1.12 | 24.7 | 74.9 | 20.7 | 0.042 | 23.53 |
| | Reverse | 1.11 | 24.7 | 78.9 | 21.6 | | |
| Spiro-OMeTAD | Forward | 1.15 | 24.8 | 82.8 | 23.7 | 0.008 | 23.74 |
| | Reverse | 1.15 | 24.9 | 83.3 | 23.9 | | |

tained from the *J*–*V* measurements within 5% deviation, demonstrating the reliability of their photovoltaic performance. Meanwhile, the steady-state power output of the three HTMs based devices at the maximum power point (MPP) were also recorded (Fig. S20 in Supporting information). O–CBz, S-CBz, and SO2-CBz based devices have the steady-state PCEs of 23.22%, 24.86%, and 21.56%, respectively, matching well with the testing results and illustrating the accuracy of the *J*-*V* test.

To analyze the effect of charge-carrier separation and transport processes in HTMs with different cores, steady-state photoluminescence (PL) and time-resolved photoluminescence (TRPL) (Fig. 2e) spectra were measured. The bare perovskite shows strong PL emission at 799 nm (Fig. 2d), while the perovskite with HTMs exhibits a significantly reduced PL intensity and shows a slight blue shift, indicating that HTMs facilitate hole extraction and also passivate perovskite surface traps. The hole-quenching ability of HTMs follows the order: S-CBz > Spiro-OMeTAD > O–CBz > SO2-CBz, which indicates that S-CBz has the strongest hole-transporting ability. Furthermore, the biexponential fitting of TRPL data suggests that the mean carrier life of the S-CBz-based PSC device decreased from 306.66 ns for the original perovskite sample to 58.8 ns, which is shorter than the mean carrier life (66.57 ns) of the Spiro-OMeTAD-based PSC device (Table S5 in Supporting information). The more efficient perovskite to S-CBz hole extraction could be attributed to the better interaction between S and Pb in perovskite and the smoother thin film morphology of the HTL layer that inhibits charge recombination.

To elucidate charge-transport dynamics in PSCs with different HTMs, electrochemical impedance spectroscopy (EIS), light intensity-dependent measurements, and dark current measurements were performed. Typical Nyquist plots for applied bias voltage ($V_{app} = 1.2$ V) are shown in Fig. 2f and were fitted using an

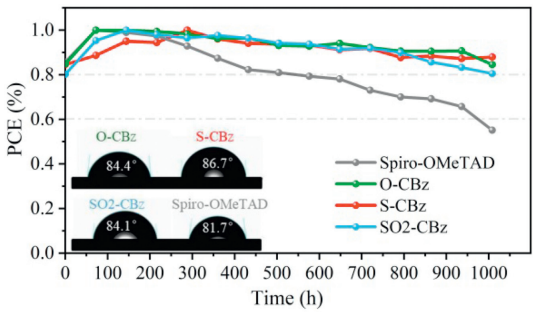


**Fig. 3.** Normalized stability of the PSCs based on O–CBz, S-CBz, SO2-CBz and Spiro-OMeTAD measured under ambient condition (30% ± 5% humidity, room temperature), the inset shows the water contact angle on different HTM surfaces after 60 s of droplet fall.

equivalent circuit model (Fig. S21 in Supporting information). The $R_{rec}$ of the S-CBz-based PSC is 658 Ω, which is slightly higher than that of the SO2-CBz-based PSC (499 Ω), Spiro-OMeTAD-based PSC (601 Ω), and O–CBz-based PSC (530 Ω) under the same conditions, indicating that the S-CBz based PSC device has less charge recombination at the perovskite/HTL interface [40]. This is consistent with light intensity-dependent measurements shown in Fig. 2g, in which the S-CBz-based PSC has the smallest slope. Fig. 2h compares the dark currents of PSC devices based on different HTMs, and the PSC based on S-CBz exhibits a lower dark current in the region from 0.6 V to 1.0 V, indicating that it has a lower leakage current compared to devices based on other HTMs. Furthermore, we investigated the defect state density at the perovskite/HTL interface by fabricating hole-only device with a structure of ITO/PEDOT:PSS/perovskite/S-CBz/Au (Fig. 2i). The defect filling limit voltage of the S-CBz-based hole-only device was 0.97 V, which is lower than that of the hole-only devices prepared by the same method using O–CBz, SO2-CBz, and Spiro-OMeTAD (Figs. S22a-c in Supporting information). The calculated defect state densities of the hole-only devices based on O–CBz, S-CBz, SO2-CBz, and Spiro-OMeTAD were $1.52 \times 10^{16}$, $1.36 \times 10^{16}$, $1.56 \times 10^{16}$, and $1.43 \times 10^{16}$ $cm^{-3}$, suggesting that the S-CBz-based PSC has greater charge recombination resistance and more efficient charge transport.

In the preparation of the molecules under investigation, we found that they exhibit certain solubility in common solvents. The hydrophobicity of these molecules coated on perovskite was further investigated by water contact angle measurements (Fig. 3 and Fig. S23 in Supporting information). After spin-coating the HTMs, the contact angle of the O–CBz-based film (86.7°) is larger than that of the S-CBz-based film (84.4°), and the contact angle is (84.1°) after SO2-CBz is spin-coated on the perovskite. The contact angles of the three HTMs are much larger than that of Spiro-OMeTAD (81.7°). It is speculated that PSC devices based on the three HTMs may have good hydrophobic properties. The larger the contact angle, the more perovskite can be prevented from being destroyed by moisture. At the same time, we tracked changes in the top morphology of unencapsulated PSCs based on O–CBz, S-CBz, SO2-CBz, and Spiro-OMeTAD during aging (Fig. S24 in Supporting information). By comparing film morphology before and after four weeks, it can be found that S-CBz has a more stable film morphology, and the film morphology of O–CBz and SO2-CBz is significantly damaged after long-term aging. Stable film morphology and excellent hydrophobic properties will jointly affect the stability of the device. To fully investigate the stability of PSCs based on different HTMs, the environmental stability of unencapsulated PSCs based on O–CBz, S-CBz, and SO2-CBz was monitored under ambient conditions of 40%–60% RH, 20–25 °C, while PSCs based on Spiro-OMeTAD were fabricated as a reference (Fig. 3). After storage in the ambient atmosphere for 1000 h, the S-CBz-based PSC retained 87% of its initial PCE and the PSCs based on SO2-CBz and O–CBz exhibited slightly poorer stability, while the Spiro-OMeTAD-based device retained only about 55%.

In this work, we developed D-$\pi$-D type a series of hole transporting materials with dibenzo-heterocycles core, named O–CBz, S-CBz, and SO2-CBz. Compared with SO2-CBz and O–CBz containing sulfone with weaker electron donor capacity than the sulfur atom, S-CBz composed of electron donor sulfur atoms is endowed with superior optoelectronic, thermal, and electrochemical properties. Notably, solar cells based on S-CBz, O–CBz exhibit excellent stability under multiple stresses. The n-i-p PSCs based on S-CBz achieved higher efficiencies (25.0%) than PSCs with SO2-CBz and O–CBz, and outperformed PCE (23.9%) with Spiro-OMeTAD. Meanwhile, the interaction strength between the three HTMs and $PbI_2$ was investigated by $^1H$ NMR and FTIR, revealing that S-CBz interacts more strongly with $PbI_2$ than O–CBz and SO2-CBz, which provides a promising design principle for HTMs.

## Declaration of competing interest

The authors declare the following financial interests/personal relationships which may be considered as potential competing interests:

Cheng Chen and Ming Cheng reports financial support was provided by National Natural Science Foundation of China. Ming Cheng reports financial support was provided by Natural Science Foundation of Jiangsu Province. If there are other authors, they declare that they have no known competing financial interests or personal relationships that could have appeared to influence the work reported in this paper.

## CRediT authorship contribution statement

**Yajie Yang:** Writing – original draft, Methodology, Investigation, Formal analysis, Data curation. **Mengde Zhai:** Investigation, Formal analysis, Data curation. **Haoxin Wang:** Writing – review & editing, Formal analysis. **Cheng Chen:** Writing – review & editing, Supervision, Investigation, Funding acquisition, Data curation. **Ziyang Xia:** Investigation, Formal analysis. **Chengyang Liu:** Investigation, Formal analysis. **Yi Tian:** Writing – review & editing, Investigation, Formal analysis. **Ming Cheng:** Writing – review & editing, Supervision, Investigation, Funding acquisition.

## Acknowledgments

This work was financially supported by the financial support from the National Natural Science Foundation of China (Nos. 22279046, 22179053), Natural Science Excellent Youth Foundation of Jiangsu Province (No. BK20220112), Special Foundation for Carbon Peak Carbon Neutralization Technology Innovation Program of Jiangsu Province (No. BE2022026–2). We also thank Ms. Tan Meihong from Shiyanjia Lab (www.shiyanjia.com) for providing invaluable assistance with the ultraviolet photoelectron spectroscopy (UPS) analysis.

## Supplementary materials

Supplementary material associated with this article can be found, in the online version, at doi:10.1016/j.cclet.2024.110700.

## References

[1] C.H. Chen, S.N. Cheng, F. Hu, et al., Adv. Mater. 66 (2024) e2403038.
[2] S. Sidhik, I. Metcalf, W. Li, et al., Science 384 (2024) 1227–1235.
[3] J. Park, J. Kim, H.S. Yun, et al., Nature 616 (2023) 724–730.
[4] Q. Lai, R. Zhuang, K. Zhang, et al., Angew. Chem. Int. Ed. 62 (2023) e202305670.

[5] E. Aktas, N. Phung, H. Köbler, et al., Energy Environ. Sci. 14 (2021) 3976–3985.
[6] L. Yuan, W. Zhu, Y. Zhang, et al., Energy Environ. Sci. 16 (2023) 1597–1609.
[7] National Renewable Energy Laboratory (NREL), Best Research Cell Efficiencies, https://www.nrel.gov/pv/cell-efficiency.htm, 2024.
[8] X. Ding, M. Yan, C. Chen, et al., Angew. Chem. Int. Ed. 63 (2024) e202317676.
[9] J. Peng, F. Kremer, D. Walter, et al., Nature 601 (2022) 573–578.
[10] V. Kumar, D. Kumar, R.D. Chavan, et al., J. Mater. Chem. A 12 (2024) 8370–8380.
[11] M. Zhai, L. Ma, C. Cai, et al., Adv. Funct. Mater. 34 (2024) 2315428.
[12] R. Zhao, T. Wu, Y. Hua, Y. Wang, Chin. Chem. Lett. 36 (2025) 109587.
[13] W. Ling, F. Liu, Q. Li, Z. Li, J. Mater. Chem. A 9 (2021) 18148–18163.
[14] H. Zhang, C. Zhao, J. Yao, W.C.H. Choy, Angew. Chem. Int. Ed. 62 (2023) e202219307.
[15] G. Du, L. Yang, C. Zhang, et al., Adv. Energy Mater. 12 (2022) 2103966.
[16] X. Zhang, X. Liu, N. Wu, et al., J. Energy Chem. 67 (2022) 19–26.
[17] H. Wang, M. Zheng, C. Chen, et al., Chem. Eng. J. 438 (2022) 135410.
[18] J. Zhang, Q. Sun, Q. Chen, et al., Adv. Funct. Mater. 29 (2019) 1900484.
[19] S. Wang, T. Wu, J. Guo, et al., ACS Cent. Sci. 6 (2024) 4c00416.
[20] X. Yu, F. Wu, X. Sun, et al., Chin. Chem. Lett. 35 (2024) 109821.
[21] T. Liu, Y. Liu, X. Gao, J. Cao, Chin. Chem. Lett. 34 (2023) 107883.
[22] Y. Ren, Y. Wei, T. Li, et al., Science 16 (2023) 3534–3542.
[23] X. Liu, B. Ding, M. Han, et al., Angew. Chem. Int. Ed. 62 (2023) e202304350.
[24] D.W. Kim, K.H. Choi, S.H. Hong, et al., Adv. Energy Mater. 13 (2023) 2300219.
[25] T. Qin, F. Wu, D. Ma, et al., ACS Mater. Lett. 2 (2020) 1093–1100.
[26] F. Meng, Y. Wang, Y. Wen, et al., Sol. RRL 4 (2020) 2000327.
[27] X. Sun, H. Fan, X. Xu, et al., Mater. Chem. Front. 8 (2024) 2764–2774.
[28] G. You, L. Li, S. Wang, Adv. Energy Mater. 12 (2022) 2102697.
[29] T. Qin, F. Wu, L. Zhu, et al., Org. Electron. 100 (2022) 106325.
[30] T. Qin, F. Wu, Y. Mu, et al., Sci. China Chem. 64 (2020) 127–133.
[31] I. García-Benito, I. Zimmermann, J. Urieta-Mora, et al., Adv. Funct. Mater. 28 (2018) 1801734.
[32] P. Huang, S.K Manju, et al., ACS Appl. Mater. Interfaces 13 (2021) 33311–33320.
[33] X. Li, W. Zhang, X. Guo, et al., Science 375 (2022) 434–437.
[34] M.W. An, B. Li, B.W. Chen, et al., Chem. Eng. J. 470 (2023) 144056.
[35] J. Zhang, Q. Sun, Q. Chen, et al., Sol. RRL. 4 (2019) 1900421.
[36] H. Zhang, X. Yu, M. Li, et al., Angew. Chem., Int. Ed. 62 (2023) e202314270.
[37] Q. Cheng, H. Chen, W. Chen, et al., Angew. Chem. Int. Ed. 62 (2023) e202312231.
[38] J. Jeong, T. Chawanpunyawat, M. Kim, et al., Adv. Energy Mater. 20 (2024) 202401965.
[39] V. Joseph, J. Xia, A.A. Sutanto, et al., ACS Appl. Mater. Interfaces 14 (2022) 22053–22060.
[40] W. Zhao, H. Lin, Y. Li, et al., Adv. Funct. Mater. 32 (2022) 2112032.